
–SUPPORTING INFORMATION–

PROPENSITY OF WATER SELF-IONS AT AIR(OIL)-WATER INTERFACES REVEALED BY DEEP POTENTIAL MOLECULAR DYNAMICS WITH ENHANCED SAMPLING

Pengchao Zhang¹, and Xuefei Xu^{1,*}.

¹Center for Combustion Energy, Department of Energy and Power Engineering, and Key Laboratory for Thermal Science and Power Engineering of Ministry of Education, Tsinghua University, Beijing 100084, China

*Corresponding author e-mail: xuxuefei@tsinghua.edu.cn

1 Computational methods

1.1 Potential model generation

1.1.1 Constructing data sets

The key to effective model training lies in constructing appropriate data sets. In this work, we aim to train two distinct models as shown in the simulation workflow (Fig. S1): a deep potential (DP) model for molecular dynamics simulations investigating water autoionization and double-layer distribution of self-ions in interfaces, and a deep Kohn-Sham (DeePKS) model with accuracy comparable to the M06-2X functional, which will be used for labeling the training data sets of energies and atomic forces. To ensure diverse and uncorrelated data, we generate multiple independent MD simulations with enhanced sampling on some configuration subsystems (Table S1), including reactive processes.

The training sets for the two models differ significantly in size due to variations in their descriptors. Both models, however, adhere to the criteria of physical symmetry and locality. The DP model incorporates angular and radial atomic environment descriptors, while the DeePKS model includes gauge invariance symmetry and density matrices projected on atomic orbitals.¹⁻³ Consequently, the DeePKS model requires only a few hundred configurations for training, whereas the DP model necessitates tens of thousands to accurately capture reactive processes as shown in Tables S4.

1.1.2 Density functional theory (DFT) calculation

The preparation of training and test data sets for DeePKS involves using the CP2K package⁴ to calculate M06-2X⁵ energies and forces. These calculations utilize Goedecker-Teter-Hutter pseudopotentials^{6,7} and a QZV3P basis set.⁸ The multi-grid level employs a plane-wave cutoff of 1000 Ry for the total density and 70 Ry for the Kohn-Sham orbitals, as confirmed by a previous convergent test.⁹ To speed up the convergence of self-consistent field (SCF) iterations, the auxiliary density matrix method is employed.¹⁰

1.1.3 DeePKS model training

We aim to perform highly accurate simulations of energy and forces using the M06-2X functional.⁵ However, the computational cost of single-point calculations at the M06-2X level is prohibitively high for our current subsystems.

To address this, we employ DeePKS, a neural network framework that trains a correction term to bridge the gap between the M06-2X target energy ($E_{\text{M06-2X}}$) and the more affordable PBE baseline energy (E_{PBE}).¹¹

The DeePKS model is generated iteratively using the DeePKS-kit.^{2,12,13} We alternate between training the correction network from the PBE baseline to the M06-2X target and solving the resulting DeePKS model using ABACUS.^{3,14,15} ABACUS employs optimized norm-conserving Vanderbilt pseudopotentials¹⁶ and a numerical atomic orbital basis.¹⁷ The calculations utilize a kinetic energy cutoff of 100 Ry and a density error SCF convergence threshold of 1×10^{-7} Ry.

The DeePKS model employs descriptors derived from projected density matrices, which are obtained using a predefined set of projectors with a maximum angular momentum of 2. The number of Bessel functions is determined based on radial and wavefunction cutoffs of 5 Bohr and 100 Ry, respectively. The model architecture consists of three hidden layers with 32 neurons each, and the "gelu" activation function is applied between the hidden layers. The training process involves 10,000 iterations with a learning rate ranging from 1×10^{-4} to 1×10^{-7} . During training processes, energy and atomic forces are estimated using a weighted mean squared loss function, i.e., $\mathcal{L}^{\text{DeePKS}}$

$$\mathcal{L}^{\text{DeePKS}} = |E^{\text{M06-2X}} - E^{\text{DeePKS}}(\varphi_i|w)|^2 + p |\mathbf{F}^{\text{M06-2X}} - \mathbf{F}^{\text{DeePKS}}(\varphi_i|w)|^2. \quad (\text{S1})$$

The Hamiltonian, denoted as \hat{H}^{DeePKS} , determines the energy and force in the DeePKS model.

$$\hat{H}^{\text{DeePKS}} = \hat{H}^{\text{PBE}} + \hat{H}^{\delta}. \quad (\text{S2})$$

\hat{H}^{DeePKS} consists of a baseline term, \hat{H}^{PBE} , and a correction term, \hat{H}^{δ} . The eigenstate of \hat{H}^{DeePKS} , represented by φ_i , partially depends on \hat{H}^{δ} . \hat{H}^{δ} is determined using projected density matrices, localized orbitals, and the DeePKS descriptor. The iterative process of combining \hat{H}^{DeePKS} with \hat{H}^{δ} identifies different ground states and achieves convergence through model training and SCF solution.^{2,3} Additionally, w represents the parameter of the neural network, and p serves as a pre-factor to compensate for errors.

Once the DeePKS model is trained, the iterative process is no longer required. Total energies and forces can be obtained through single-point calculations using the PBE functional corrected for the E_{δ} term. The PBE-based DeePKS model shows good agreement with independent testing data obtained from M06-2X/QZV3P calculations, with low root mean square errors (RMSEs) of 0.49 meV/atom in energy and 46 meV/Å in force (Fig. S4). Additionally, the PBE-based DeePKS model offers significant computational efficiency, saving nearly nine times the time compared to the standard M06-2X functional (Table S3).

Find further information on DeePKS-kit at the website.¹⁸

1.1.4 DP model training

The Deep Potential Smooth Edition (DeepPot-SE) descriptor^{1,19} is utilized in this study. The embedding net is configured with layer sizes of [25, 50, 100] and employs a "tanh" activation function between hidden layers. A submatrix size of 16 is incorporated. The neighbor atom cutoff radius is set at 6.0 Å, with smoothing starting at 0.5 Å. The maximum number of neighboring atoms for H, C, and O atoms is specified as [88, 46, 45] respectively. The embedding net is followed by the fitting net, comprising layers sized at [240, 240, 240], where the "tanh" activation function is applied between hidden layers. The fitting net incorporates the ResNet architecture.²⁰ The training process consists of 10 million steps with a learning rate ranging from 1×10^{-3} to 1×10^{-8} . The loss function, denoted as \mathcal{L}^{DP} , combines energy and atomic forces using a weighted mean square approach

$$\mathcal{L}^{\text{DP}} = \frac{p_e}{N} |E^{\text{DeePKS}} - E^{\text{DP}}(w)|^2 + \frac{p_f}{3N} \sum_{i\alpha} |F_{i\alpha}^{\text{DeePKS}} - F_{i\alpha}^{\text{DP}}(w)|^2, \quad (\text{S3})$$

where N denotes the number of atoms, p_e and p_f are pre-factors of the energy E and force F , respectively, and w represents the parameter of the neural network. $F_{i\alpha}$ represents the force felt by atom i in the direction of α th. Once the final DP model training is complete, it is compressed for efficient execution of MD simulations.²¹

The DP model is trained using the DeePMD-kit^{22,23} and a training data set in approximate M06-2X accuracy. A total of 69,787 configurations are used for accurate results. The trained DP model is then evaluated by testing its predictions on a separate data set, in which the energies and forces are obtained by standard M06-2X calculations. The DP model achieves energy RMSE of 0.85 meV/atom and atomic force RMSE of 58 meV/Å (Fig. S5), demonstrating

a level of precision comparable to M06-2X. Furthermore, the DP model exhibits a computational speed advantage of five orders of magnitude over M06-2X-based simulations (Table S3).

Find further information on DeepMD-kit at the website.²⁴

1.2 Molecular dynamics simulations

1.2.1 MD simulation for generating data set configurations

The configurations (subsystems B-H in Table S1) are obtained through MD simulations using CP2K,⁴ with the exception of some pure water configurations (subsystem A in Table S1) taken from previous work.²⁵ To speed up the sampling process, the semi-empirical method GFN1-xTB²⁶ is employed. The MD simulations are carried out in a constant volume constant temperature (NVT) ensemble with a time step of 1.0 fs, maintained using a velocity rescaling thermostat²⁷ at 300 K with a damping time of 0.2 ps.

1.2.2 DPMD simulation for studying the autoionization and the double-layer distribution

To investigate the double-layer of self-ions at water interfaces, DPMD simulations are conducted using the LAMMPS software.²⁸ Prior to simulating the interface systems, the accuracy of water autoionization in a system containing 58 H₂O (water bulk 1 in Table S2) is assessed through 10 ns NVT simulations with a 1.0 fs integration time step. To test the effect of box size as shown in Fig. S7, we also conduct an autoionization simulation on a system containing 256 H₂O (water bulk 2 in Table S2) with 1 ns. Temperature control at 300 K is achieved using a velocity rescaling thermostat with a damping time of 0.04 ps. For the air-water and oil-water interface systems (Table S2), 30 ns simulations are performed to obtain converged results, and other simulation settings are consistent with those used for water bulk systems.

1.3 Enhanced sampling settings

1.3.1 Bias potential of enhanced sampling

In MD simulations for constructing the data sets and the DPMD simulations for studying the autoionization and the double-layer distribution, the OPES method²⁹⁻³¹ with collective variables (CVs) is employed. The CVs, denoted as $\mathbf{s}(\mathbf{R})$, effectively capture slow modes and infrequent occurrences by relating them to atomic coordinates \mathbf{R} . The external bias potential $V(\mathbf{s})$ is incorporated into the system's potential energy $U(\mathbf{R})$ during MD simulations using the PLUMED plugin.³² In OPES, $V(\mathbf{s})$ at the n th step is characterized by

$$V_n(\mathbf{s}) = \left(1 - \frac{1}{\gamma}\right) \frac{1}{\beta} \log\left(\frac{P_n(\mathbf{s})}{Z_n} + \epsilon\right), \quad (\text{S4})$$

where the expression involves the bias factor $\gamma = \beta \Delta E_{\text{bias}}$, inverse Boltzmann factor $\beta = 1/k_B T$, the unbiased marginal distribution probability $P(\mathbf{s})$, and a normalization factor Z . The regularization term $\epsilon = e^{-\gamma/(1-1/\gamma)}$ ensures a positive argument for the logarithm and imposes a bias constraint that confines sampling to the specified region of interest. The adaptive kernel width is used to update the bias every 500 steps, and a value of ΔE_{bias} of 75 kJ/mol is chosen to approximate the free energy barrier of water autoionization.

The OPES-explore variant is employed for collecting data set configurations, as it facilitates phase space exploration in systems containing water (subsystems B-F in Table S1), while OPES with expanded ensembles target distribution³¹ is used to explore the phase space of pure oil subsystems G and H (Table S1). During the final DPMD simulations, the original OPES method generates well-converged free energy estimates (the systems as shown in Table S2). The difference in estimating probability distributions between OPES and OPES-explore arises due to their distinct approaches, although they share the concept of defining the bias potential. OPES calculates an unbiased probability $P(\mathbf{s})$ on-the-fly using weighted kernel density estimation (KDE), while OPES-explore calculates a well-tempered probability $p^{\text{WT}}(\mathbf{s}) \propto [P(\mathbf{s})]^{\frac{1}{\gamma}}$ based on an averaged KDE.^{29,30}

1.3.2 Definition of collective variables

Protons are able to diffuse through water utilizing the Grotthuss mechanism,^{25,33,34} in which a charge defect migrates through the hydrogen network rather than a specific proton. Therefore, any CV related to proton diffusion must be able to identify charge defects without reference to particular atomic coordinates. In this particular case, there are

various possible charge defects, namely the two water self-ions H_3O^+ and OH^- . To automatically identify these charge defects, we implement the methodology proposed in References^{9,35,36} which involves tessellation of the space by Voronoi polyhedra centered on the O atoms and subsequent summation of the contained charge in each polyhedron. If the charge within a polyhedron differs from zero, we attribute the charge deficiency to the O atom located at the center of the polyhedron.

To calculate the number of hydrogen (H) atoms n_i centered on oxygen (O) atom i , utilize the specified equation

$$n_i = \sum_{j=1}^{\text{Num}_H} \frac{e^{-\lambda|\mathbf{R}_i - \mathbf{R}_j|}}{\sum_{m=1}^{\text{Num}_O} e^{-\lambda|\mathbf{R}_m - \mathbf{R}_j|}}, \quad (\text{S5})$$

where m represents the index of all Voronoi centers, and the sum includes all H atoms with index j . The parameter λ governs the smoothness of the function.

The charge defect of the Voronoi center, δ_i , is calculated by subtracting the reference number, n_i^0 (protons for the atom at the polyhedron center), from the H number, n_i

$$\delta_i = n_i - n_i^0, \quad (\text{S6})$$

where we assume $n_i^0 = 2$ for the O atom in water.

During OPES simulations to study water autoionization processes, the CV \mathbf{s}_a with a value of $\lambda = 5$ is utilized to obtain a smoother definition of the self-ion number, given that water self-ions (H_3O^+ and OH^-) may be present.

$$\mathbf{s}_a = \sum_{i=1}^{\text{Num}_O} \delta_i^2, \quad (\text{S7})$$

where the process encourages autoionization in which the value of \mathbf{s}_a ranges from 0 to <2 .

The mean absolute error (MAE) between $\mathbf{s}_a^{\lambda=5}$ and $\mathbf{s}_a^{\lambda=100}$ is calculated. Although $\mathbf{s}_a^{\lambda=5}$ deviates slightly from 2 due to the smoothness of the function for well sampling, $\mathbf{s}_a^{\lambda=100}$ is much closer to 2 at autoionization state. However, $\mathbf{s}_a^{\lambda=100}$ is too narrow for effective sampling and reweighting. The MAE value of approximately 0.7 indicates that when $\mathbf{s}_a^{\lambda=5} \approx 1.3$ and $\mathbf{s}_a^{\lambda=100} \approx 2.0$, they represent a pair of H_3O^+ and OH^- coexisting in water.

Furthermore, we introduce a CV \mathbf{s}_t with a value of $\lambda = 8$ that indicates the self-ion distance between H_3O^+ and OH^-

$$\mathbf{s}_t = - \sum_{i=1}^{\text{Num}_O} \sum_{j>i}^{\text{Num}_O} r_{i,j} \delta_i \delta_j, \quad (\text{S8})$$

while \mathbf{s}_t can differentiate between the state of pure water ($\mathbf{s}_t \approx 0 \text{ \AA}$) and the state of autoionization ($\mathbf{s}_t > 0 \text{ \AA}$), prior to the formation of the contact OH^- and H_3O^+ ion pair ($\mathbf{s}_t = 2.5 \text{ \AA}$ in Fig. 2b), the \mathbf{s}_t value resolution around the initial transfer of proton ($0 < \mathbf{s}_t < 2.5 \text{ \AA}$) is insufficient due to its concentration around zero. Therefore, we employ the piecewise logarithmic function

$$\mathbf{s}'_t = \begin{cases} \log(\mathbf{s}_t + \epsilon), & 0 \leq \mathbf{s}_t < 1, \\ \mathbf{s}_t - 1 + \log(1 + \epsilon), & \mathbf{s}_t \geq 1, \end{cases} \quad (\text{S9})$$

where $\epsilon = 0.03$ represents the regularization term. The self-ion distance variant \mathbf{s}'_t can differentiate between the pure water state ($\mathbf{s}'_t \approx -3 \text{ \AA}$), the transition state ($\mathbf{s}'_t \approx 0 \text{ \AA}$), and the autoionization state ($\mathbf{s}_t > 1 \text{ \AA}$).

Based on the definition of self-ion number \mathbf{s}_a , we designed the z-axis coordinate (the interface normal vector is parallel to the z-axis direction) of H_3O^+ and OH^- to explore their preferences along the interface after water autoionization.

For the negative ion (OH^-), we represent the CV of the z-axis coordinate as \mathbf{s}_{zn}

$$\mathbf{s}_{zn} = \sum_{i=1}^{\text{Num}_O} \delta z_i \delta_i^2 \quad (\text{for } \delta_i < 0). \quad (\text{S10})$$

For the positive ion (H_3O^+), the z-axis coordinate CV represented by the \mathbf{s}_{zp}

$$\mathbf{s}_{zp} = \sum_{i=1}^{\text{Num}_O} \delta z_i \delta_i^2 \quad (\text{for } \delta_i > 0), \quad (\text{S11})$$

where $\delta z_i = |z_i - z_{\text{mid}}|$ indicates that we calculate the absolute value with respect to the central layer ($z_{\text{mid}} = 53$ Å is the middle value of the box along the z-axis) in our interface systems, which combines the top and bottom interfaces to determine the CV values. Note that the free energy curves are plotted as functions of s_{zn} and s_{zp} in manuscript Fig. 2. Here, we reference the interface position as the zero point for s_{zn} and s_{zp} to better understand their locations relative to the interface. In other words, s_{zn} and s_{zp} values (in Eq. S10 and S11) are adjusted by subtracting a constant representing interface thicknesses to align the interface position at zero. This adjustment does not alter the free energy curves but results in a shift along the x-axis.

When reweighting the unbiased possibility, we focus solely on the formation of one pair of self-ions through pure water ($0 < s_a \leq 2$). We do not consider cases where autoionization results in the formation of more than one pair of self-ions ($s_a > 2$) when calculating the free energy along the CVs s_{zn} and s_{zp} .

The uncertainty is calculated for $s_{zn}^{\lambda=5}$ and $s_{zn}^{\lambda=100}$, as well as for $s_{zp}^{\lambda=5}$ and $s_{zp}^{\lambda=100}$, in both the oil-water and air-water systems. In the oil-water system, the MAE value is found to be ~ 10 Å. In the air-water system, the MAE value is ~ 9 Å. This implies that the curves depicted in manuscript Fig. 2 exhibit a horizontal displacement along the x-axis within the specified range due to the smoothness of the CVs for good sampling.

1.3.3 Free energy calculation

Upon completion of the DPMD simulation, the free energy surface (FES) along the CV can be calculated as follows

$$F(\mathbf{s}) = -\frac{1}{\beta} \log P(\mathbf{s}). \quad (\text{S12})$$

In the regime of quasi-static bias, $P(\mathbf{s})$ can be reweighted as an average over the biased ensemble.²⁹

$$P(\mathbf{s}) = \frac{\langle \delta[\mathbf{s} - \mathbf{s}(\mathbf{R})] e^{\beta V(\mathbf{s})} \rangle_V}{\langle e^{\beta V(\mathbf{s})} \rangle_V}. \quad (\text{S13})$$

2 Other computational details

The diffusion coefficient of water is determined from the mean square displacement (MSD) using Einstein's relation, which was previously described.²⁵ As shown in Table S5, our M06-2X-based DPMD simulations reveal a diffusion coefficient of $2.3 \times 10^{-9} \text{ m}^2\text{s}^{-1}$ for water molecules, consistent with experimental results ($\sim 2.3 \times 10^{-9} \text{ m}^2\text{s}^{-1}$ at ~ 300 K). Additionally, the diffusion coefficients for H_3O^+ and OH^- at 300 K are 8.2×10^{-9} and $4.6 \times 10^{-9} \text{ m}^2\text{s}^{-1}$, respectively, which agree well with experimental measurements ($\sim 9.3 \times 10^{-9} \text{ m}^2\text{s}^{-1}$ for H_3O^+ and $\sim 5.3 \times 10^{-9} \text{ m}^2\text{s}^{-1}$ for OH^- at ~ 300 K). The simulation box includes 128 H_2O molecules. When analyzing OH^- or H_3O^+ , a ratio of 1 ion to 127 H_2O is used. To accurately locate OH^- or H_3O^+ , Voronoi CVs are employed due to proton hopping following the Grotthuss mechanism. DPMD simulations are conducted for 1 ns in order to perform statistical analysis.

The simulation results are presented using VMD³⁷ and Matplotlib³⁸ packages. To investigate the minimum free energy pathways derived from the two-dimensional free energy surface, we employed the Minimum Energy Path Surface Analysis (MEPSA) package.³⁹

Table S1: **Details of the subsystems for building training and test data sets.** Using OPES-explore, the oil-water subsystems B, C, D, E, and F contain water autoionization processes to include features of H_3O^+ and OH^- ions. The phase space of pure oil subsystems G and H is explored by OPES with expanded ensembles target distribution. The only exceptions are some pure water configurations (subsystem A) are added from our previous work.²⁵ Schematic diagrams of subsystem indexes are depicted in Fig. S2.

subsystem	box size (\AA^3)	no. of H_2O	no. of $\text{C}_{10}\text{H}_{22}$
A	$\sim 12.2 \times 12.2 \times 12.2$ (<i>NPT</i>)	64	0
B	$12.0 \times 12.0 \times 12.0$ (<i>NVT</i>)	58	0
C	$12.0 \times 12.0 \times 36.0$ (<i>NVT</i>)	54	0
D	$12.5 \times 12.5 \times 12.5$ (<i>NVT</i>)	44	2
E	$12.5 \times 12.5 \times 12.5$ (<i>NVT</i>)	22	4
F	$12.5 \times 12.5 \times 20.0$ (<i>NVT</i>)	52	5
G	$12.5 \times 12.5 \times 12.5$ (<i>NVT</i>)	0	6
H	$12.5 \times 12.5 \times 12.5$ (<i>NVT</i>)	0	7

Table S2: **Details of systems for performing final DPMD simulations.**

system	box size (\AA^3)	no. of H_2O	no. of $\text{C}_{10}\text{H}_{22}$
Water bulk 1	$12.0 \times 12.0 \times 12.0$	58	0
Water bulk 2	$19.7 \times 19.7 \times 19.7$	256	0
Air-water interface	$12.1 \times 12.1 \times 106.0$	256	0
Oil-water interface	$12.1 \times 12.1 \times 106.0$	256	24

Table S3: **The runtime of calculations.** DFT labeling and DeePKS labeling are executed on a CPU processor with parallelization. The runtime is designated for the completion of the self-consistent field iteration. The runtime of DPMD simulations with OPES on GPU is provided.

step	system	machine	time
DFT labeling for the DeePKS data set	subsystem B	24-core CPU	35 min/frame
DeePKS labeling for the DeePMD data set	subsystem B	24-core CPU	4 min/frame
DPMD simulation with OPES	Water bulk 1	1 Tesla A100	127 timesteps/s
DPMD simulation with OPES	Water bulk 1	1 RTX 3090	64 timesteps/s
DPMD simulation with OPES	Water bulk 2	1 RTX 3090	5 timesteps/s
DPMD simulation with OPES	Air-water interface	1 Tesla A100	80 timesteps/s
DPMD simulation with OPES	Air-water interface	1 RTX 3090	10 timesteps/s
DPMD simulation with OPES	Oil-water interface	1 Tesla A100	65 timesteps/s
DPMD simulation with OPES	Oil-water interface	1 RTX 3090	9 timesteps/s

Table S4: **The component of the training and test data sets for the DeePKS and DP models.** For subsystems A, B, D, E, G, and H, the DeePKS model is used to label the DP training data sets. For subsystems C and F, the M06-2X/QZV3P method is directly used to label the DP training data sets. The test data sets and DeePKS training data sets are all labeled using the M06-2X/QZV3P method. More details about subsystems are listed in Table S1.

subsystem	DeePKS train	DP train	DeePKS test	DP test
A, B	150	23371	680	680
C	N/A	5997	N/A	N/A
D	150	8106	500	500
E	150	8872	500	500
F	N/A	13682	N/A	N/A
G, H	150	9759	800	800
Total	600	69787	2480	2480

Table S5: **Diffusion coefficients of H_3O^+ (D^+), OH^- (D^-), and H_2O (D).**

methods	temperature (K)	D^+ (10^{-9} m ² /s)	D^- (10^{-9} m ² /s)	D (10^{-9} m ² /s)	refs
experiment	291.2	8.2	4.5		refs ^{40,41}
experiment	298.2	9.3	5.3	2.3	refs ^{40,41}
experiment	301.15	9.5	5.3		refs ⁴²⁻⁴⁴
experiment	300			2.4	ref. ⁴¹
RPBE-D3 BOMD	300 (<i>NVT</i>)	8.5	4.7	2.3	ref. ⁴¹
RPBE-D3 CPMD	300 (<i>NVT</i>)	8.4	4.3	2.3	ref. ⁴¹
PBE0-TS CPMD	330 (<i>NVT</i>)	8.3	3.7		ref. ⁴⁴
SCAN CPMD	330 (<i>NVT</i>)	5.7	2.9		ref. ⁴⁵
SCAN DPMD	300 (<i>NVT</i>)	3.6	1.4		ref. ²⁵
SCAN DPMD	330 (<i>NVT</i>)	6.0	3.0		ref. ²⁵
SCAN DPMD	330 (<i>NVT</i>)	5.8	3.2		ref. ⁴⁶
M06-2X DPMD	300 (<i>NVT</i>)	8.3	4.6	2.3	this work

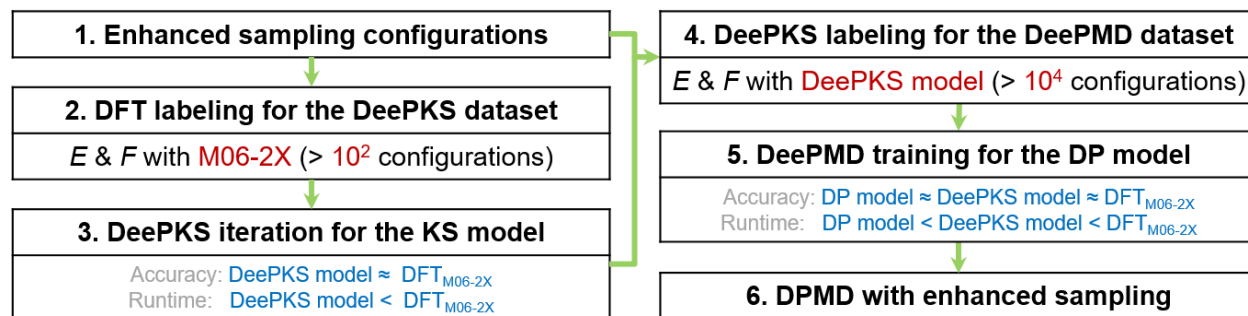


Figure S1: **Simulation workflow in detail.** The workflow involves a series of steps for efficient and accurate exploration of the double-layer distribution of water self-ions in interfaces after autoionization.

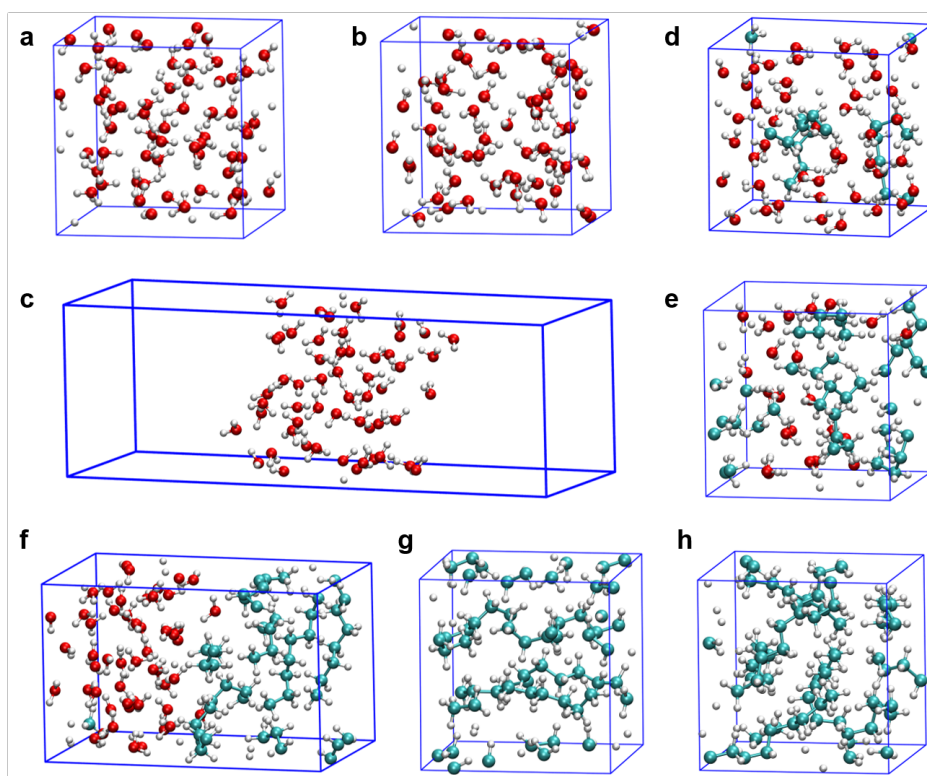


Figure S2: **Schematic diagram of subsystems in data sets.** (a) A cubic box containing H₂O linked to subsystem index A. (b) A cubic box containing H₂O, H₃O⁺, and OH⁻ linked to subsystem index B. (c) A box containing H₂O, H₃O⁺, and OH⁻ linked to subsystem index C. (d and e) A cubic box containing H₂O, H₃O⁺, OH⁻, and C₁₀H₂₂ linked to subsystem indexes D and E. (f) A box containing H₂O, H₃O⁺, OH⁻, and C₁₀H₂₂ linked to subsystem index F. (g and h) A cubic box containing C₁₀H₂₂ linked to subsystem indexes G and H. More details about these subsystems are listed in Table S1. Color code: hydrogen, white; nitrogen, blue; oxygen, red; carbon, green.

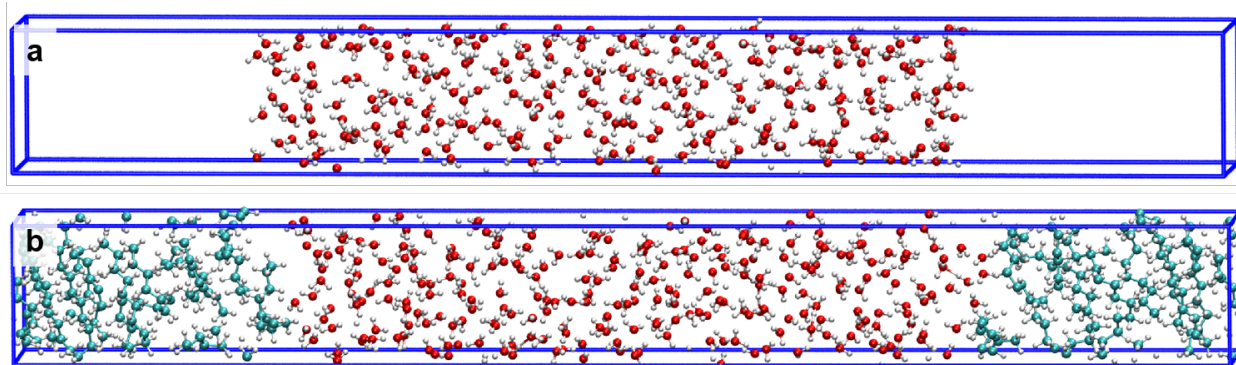


Figure S3: **Schematic diagram of interfacial systems for performing final molecular dynamics.** (a) A box linked to the air-water interface system. (b) A box linked to the oil-water interface system. More details about interfacial systems are listed in Table S2.

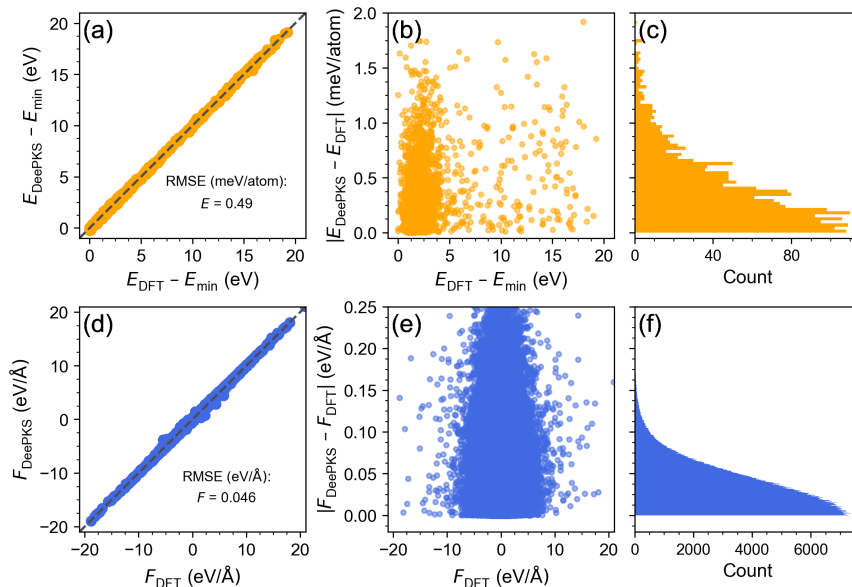


Figure S4: **Error distribution of the DeePKS model on the test data sets as listed in Table S4.** (a) The distribution of $E_{\text{DeePKS}} - E_{\text{min}}$ with respect to $E_{\text{DFT}} - E_{\text{min}}$. (b) Left: the distribution of $|E_{\text{DeePKS}} - E_{\text{DFT}}|$ with respect to $E_{\text{DFT}} - E_{\text{min}}$. (c) Right: the histogram of $|E_{\text{DeePKS}} - E_{\text{DFT}}|$. (d) The distribution of F_{DeePKS} with respect to F_{DFT} . (e) Left: the distribution of $|F_{\text{DeePKS}} - F_{\text{DFT}}|$ with respect to F_{DFT} . (f) Right: the histogram of $|F_{\text{DeePKS}} - F_{\text{DFT}}|$. Here, E_{DFT} and F_{DFT} are the energy and force calculated by the M06-2X functional; E_{DeePKS} and F_{DeePKS} are the energy and force performed by the present DeePKS model; and E_{min} is the minimum absolute energy in the test data set.

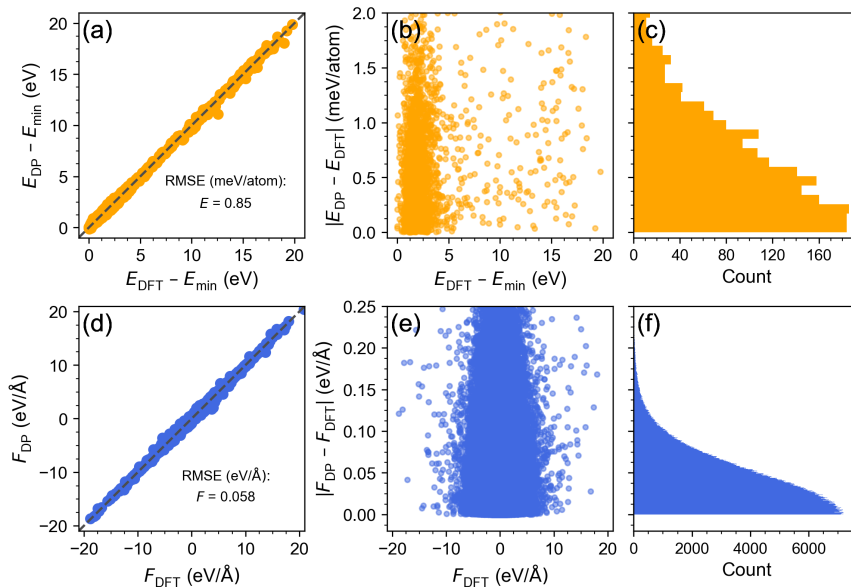


Figure S5: **Error distribution of the DP model on the test data sets as listed in Table S4.** (a) The distribution of $E_{DP} - E_{\min}$ with respect to $E_{DFT} - E_{\min}$. (b) Left: the distribution of $|E_{DP} - E_{DFT}|$ with respect to $E_{DFT} - E_{\min}$. (c) Right: the histogram of $|E_{DP} - E_{DFT}|$. (d) The distribution of F_{DP} with respect to F_{DFT} . (e) Left: the distribution of $|F_{DP} - F_{DFT}|$ with respect to F_{DFT} . (f) Right: the histogram of $|F_{DP} - F_{DFT}|$. Here, E_{DFT} and F_{DFT} are the energy and force calculated by the M06-2X functional; E_{DP} and F_{DP} are the energy and force performed by the present DP model; and E_{\min} is the minimum absolute energy in the test data set.

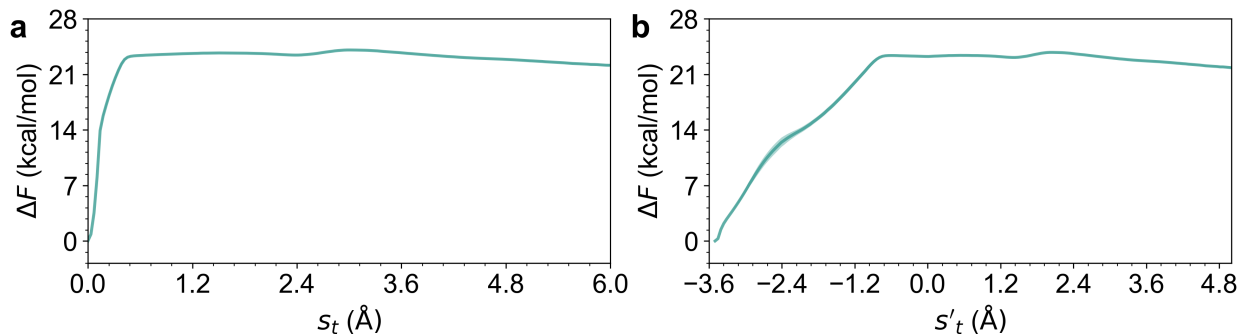


Figure S6: **Water autoionization in water bulk system.** One-dimensional projections of the FES along the CVs (a) s_t and (b) s'_t . The CVs s'_t and s_t are not sufficient to illustrate the metastable state when ions separate from each other, so we primarily focus on the FES along the self-ion number s_a as shown in the manuscript.

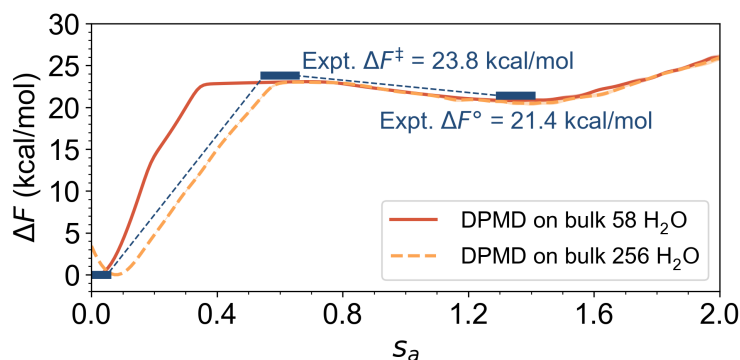


Figure S7: **Water autoionization in bulk systems.** One-dimensional FES as a function of the self-ion number s_a in water bulk systems. The results of ΔF^\ddagger and ΔF° in different bulk water sizes containing 58 H_2O and 256 H_2O do not indicate significant size effects, consistent with the size convergence tests conducted by Liu et al.⁴⁷ Identifying transition states becomes more ambiguous in 256 H_2O due to the presence of more water molecules.

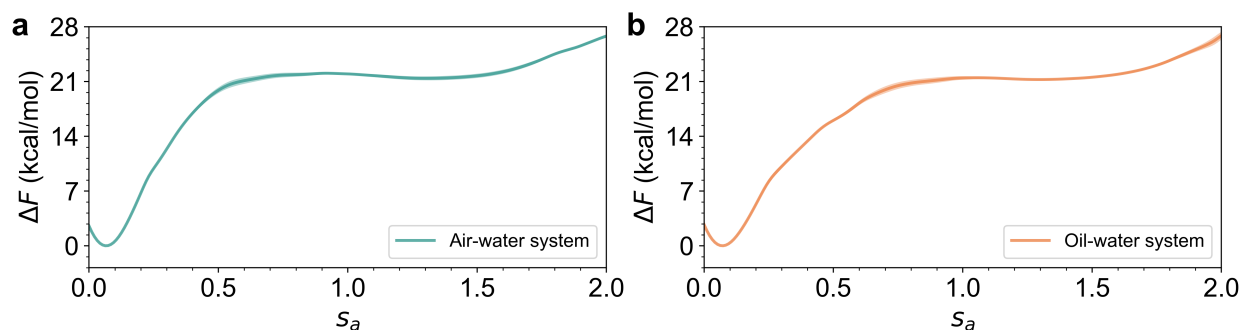


Figure S8: **Water autoionization in interface systems.** One-dimensional FES as a function of the self-ion number s_a in (a) air-water system and (b) oil-water system. Identifying transition states becomes more ambiguous in these systems due to the presence of more water molecules. The results of the reaction energy for water autoionization in 256 H_2O ($\Delta F^\circ = 21.4, 21.2$ kcal/mol in air-water, oil-water system, respectively) are consistent with those in the bulk with 58 H_2O ($\Delta F^\circ = 20.8$ kcal/mol), but the activation free energy (ΔF^\ddagger) is slightly lower than the result in bulk.

References

- [1] Zhang, L.; Han, J.; Wang, H.; Car, R.; Weinan, E. Deep Potential Molecular Dynamics: A Scalable Model With the Accuracy of Quantum Mechanics. *Phys. Rev. Lett.* **2018**, *120*, 143001.
- [2] Chen, Y.; Zhang, L.; Wang, H.; E, W. DeePKS: A Comprehensive Data-Driven Approach Toward Chemically Accurate Density Functional Theory. *J. Chem. Theory Comput.* **2020**, *17*, 170–181.
- [3] Li, W.; Ou, Q.; Chen, Y.; Cao, Y.; Liu, R.; Zhang, C.; Zheng, D.; Cai, C.; Wu, X.; Wang, H.; Chen, M.; Zhang, L. DeePKS+ABACUS as a Bridge Between Expensive Quantum Mechanical Models and Machine Learning Potentials. *J. Phys. Chem. A* **2022**, *126*, 9154–9164.
- [4] Kühne, T. D. et al. CP2K: An Electronic Structure and Molecular Dynamics Software Package-Quickstep: Efficient and Accurate Electronic Structure Calculations. *J. Chem. Phys.* **2020**, *152*, 194103.
- [5] Zhao, Y.; Truhlar, D. G. The M06 Suite of Density Functionals for Main Group Thermochemistry, Thermochemical Kinetics, Noncovalent Interactions, Excited States, and Transition Elements: Two New Functionals and Systematic Testing of Four M06-Class Functionals and 12 Other Functionals. *Theor. Chem. Acc.* **2008**, *120*, 215–241.
- [6] Goedecker, S.; Teter, M.; Hutter, J. Separable Dual-Space Gaussian Pseudopotentials. *Phys. Rev. B* **1996**, *54*, 1703.
- [7] Hartwigsen, C.; Goedecker, S.; Hutter, J. Relativistic Separable Dual-Space Gaussian Pseudopotentials from H to Rn. *Phys. Rev. B* **1998**, *58*, 3641.
- [8] VandeVondele, J.; Krack, M.; Mohamed, F.; Parrinello, M.; Chassaing, T.; Hutter, J. Quickstep: Fast and Accurate Density Functional Calculations Using a Mixed Gaussian and Plane Waves Approach. *Comput. Phys. Commun.* **2005**, *167*, 103–128.
- [9] Zhang, P.; Gardini, A. T.; Xu, X.; Parrinello, M. Intramolecular and Water Mediated Tautomerism of Solvated Glycine. *J. Chem. Inf. Model.* **2024**, *64*, 3599–3604.
- [10] Guidon, M.; Hutter, J.; VandeVondele, J. Auxiliary Density Matrix Methods for Hartree-Fock Exchange Calculations. *J. Chem. Theory Comput.* **2010**, *6*, 2348–2364.
- [11] Perdew, J. P.; Burke, K.; Ernzerhof, M. Generalized Gradient Approximation Made Simple. *Phys. Rev. Lett.* **1996**, *77*, 3865.
- [12] Chen, Y.; Zhang, L.; Wang, H.; E, W. Ground State Energy Functional With Hartree-Fock Efficiency and Chemical Accuracy. *J. Phys. Chem. A* **2020**, *124*, 7155–7165.
- [13] Chen, Y.; Zhang, L.; Wang, H.; Weinan, E. DeePKS-kit: A Package for Developing Machine Learning-Based Chemically Accurate Energy and Density Functional Models. *Comput. Phys. Commun.* **2023**, *282*, 108520.
- [14] Chen, M.; Guo, G.; He, L. Systematically Improvable Optimized Atomic Basis Sets for *Ab Initio* Calculations. *J. Phys.: Condens. Matter* **2010**, *22*, 445501.
- [15] Li, P.; Liu, X.; Chen, M.; Lin, P.; Ren, X.; Lin, L.; Yang, C.; He, L. Large-Scale *Ab Initio* Simulations Based on Systematically Improvable Atomic Basis. *Comput. Mater. Sci.* **2016**, *112*, 503–517.
- [16] Schlipf, M.; Gygi, F. Optimization Algorithm for the Generation of ONCV Pseudopotentials. *Comput. Phys. Commun.* **2015**, *196*, 36–44.
- [17] Lin, P.; Ren, X.; He, L. Strategy for Constructing Compact Numerical Atomic Orbital Basis Sets by Incorporating the Gradients of Reference Wavefunctions. *Phys. Rev. B* **2021**, *103*, 235131.
- [18] <https://deepks-kit-qj.readthedocs.io/en/latest/index.html>.
- [19] Zhang, L.; Han, J.; Wang, H.; Saidi, W.; Car, R.; E, W. End-to-End Symmetry Preserving Inter-Atomic Potential Energy Model for Finite and Extended Systems. *Adv. Neural Inf. Process. Syst.* **2018**, *31*.
- [20] He, K.; Zhang, X.; Ren, S.; Sun, J. Deep Residual Learning for Image Recognition. Proceedings of the IEEE conference on computer vision and pattern recognition. 2016; pp 770–778.
- [21] Lu, D.; Jiang, W.; Chen, Y.; Zhang, L.; Jia, W.; Wang, H.; Chen, M. DP Compress: A Model Compression Scheme for Generating Efficient Deep Potential Models. *J. Chem. Theory Comput.* **2022**, *18*, 5559–5567.
- [22] Wang, H.; Zhang, L.; Han, J.; E, W. DeePMD-kit: A Deep Learning Package for Many-Body Potential Energy Representation and Molecular Dynamics. *Comput. Phys. Commun.* **2018**, *228*, 178–184.
- [23] Zeng, J. et al. DeePMD-kit v2: A Software Package for Deep Potential Models. *J. Chem. Phys.* **2023**, *159*, 054801.
- [24] <https://docs.deepmodeling.com/projects/deepmd/en/master/index.html>.
- [25] Zhang, P.; Feng, M.; Xu, X. Double-Layer Distribution of Hydronium and Hydroxide Ions in the Air-Water Interface. *ACS Phys. Chem. Au* **2024**.
- [26] Grimme, S.; Bannwarth, C.; Shushkov, P. A Robust and Accurate Tight-Binding Quantum Chemical Method for Structures, Vibrational Frequencies, and Noncovalent Interactions of Large Molecular Systems Parametrized for All spd-Block Elements ($Z=1-86$). *J. Chem. Theory Comput.* **2017**, *13*, 1989–2009.
- [27] Bussi, G.; Donadio, D.; Parrinello, M. Canonical Sampling Through Velocity Rescaling. *J. Chem. Phys.* **2007**, *126*, 014101.
- [28] Plimpton, S. Fast Parallel Algorithms for Short-Range Molecular Dynamics. *J. Comput. Phys.* **1995**, *117*, 1–19.
- [29] Invernizzi, M.; Parrinello, M. Rethinking Metadynamics: From Bias Potentials to Probability Distributions. *J. Phys. Chem. Lett.* **2020**, *11*, 2731–2736.
- [30] Invernizzi, M.; Parrinello, M. Exploration vs Convergence Speed in Adaptive-Bias Enhanced Sampling. *J. Chem. Theory Comput.* **2022**, *18*, 3988–3996.
- [31] Invernizzi, M.; Piaggi, P. M.; Parrinello, M. Unified Approach to Enhanced Sampling. *Phys. Rev. X* **2020**, *10*, 041034.
- [32] Tribello, G. A.; Bonomi, M.; Branduardi, D.; Camilloni, C.; Bussi, G. PLUMED 2: New Feathers for an Old Bird. *Comput. Phys. Commun.* **2014**, *185*, 604–613.
- [33] de Grotthuss, C. J. T. Mémoire sur la Décomposition de l'Eau et des Corps qu'elle Tient en Dissolution à l'Aide de l'Électricité Galvanique. *Ann. Chim.* **1806**, *54*–74.
- [34] Marx, D. Proton Transfer 200 Years after von Grotthuss: Insights from *Ab Initio* Simulations. *ChemPhysChem* **2006**, *7*, 1848–1870.
- [35] Grifoni, E.; Piccini, G.; Parrinello, M. Microscopic Description of Acid-Base Equilibrium. *Proc. Natl. Acad. Sci. U. S. A.* **2019**, *116*, 4054–4057.
- [36] Grifoni, E.; Piccini, G.; Parrinello, M. Tautomeric Equilibrium in Condensed Phases. *J. Chem. Theory Comput.* **2020**, *16*, 6027–6031.
- [37] Humphrey, W.; Dalke, A.; Schulten, K. VMD: Visual Molecular Dynamics. *J. Mol. Graph.* **1996**, *14*, 33–38.
- [38] Hunter, J. D. Matplotlib: A 2D Graphics Environment. *Comput. Sci. & Eng.* **2007**, *9*, 90–95.
- [39] Marcos-Alcalde, I.; Setoain, J.; Mendieta-Moreno, J. I.; Mendieta, J.; Gomez-Puertas, P. MEPSA: Minimum Energy Pathway Analysis for Energy Landscapes. *Bioinformatics* **2015**, *31*, 3853–3855.
- [40] Hardy, E. H.; Zygari, A.; Zeidler, M. D.; Holz, M.; Sacher, F. D. Isotope Effect on the Translational and Rotational Motion in Liquid Water and Ammonia. *J. Chem. Phys.* **2001**, *114*, 3174–3181.
- [41] Muñoz-Santiburcio, D. Accurate Diffusion Coefficients of the Excess Proton and Hydroxide in Water via Extensive *Ab Initio* Simulations with Different Schemes. *J. Chem. Phys.* **2022**, *157*.
- [42] Halle, B.; Karlström, G. Prototropic Charge Migration in Water. Part 2.—Interpretation of Nuclear Magnetic Resonance and Conductivity Data in Terms of Model Mechanisms. *J. Chem. Soc. Faraday Trans. 2: Mol. Chem. Phys.* **1983**, *79*, 1047–1073.
- [43] Sluyters, J.; Sluyters-Rehbach, M. The Mechanism of the Hydrogen Ion Conduction in Liquid Light and Heavy Water Derived from the Temperature Dependence of Their Limiting Conductivities. *J. Phys. Chem. B* **2010**, *114*, 15582–15589.
- [44] Chen, M.; Zheng, L.; Santra, B.; Ko, H.-Y.; DiStasio Jr, R. A.; Klein, M. L.; Car, R.; Wu, X. Hydroxide Diffuses Slower Than Hydronium in Water Because Its Solvated Structure Inhibits Correlated Proton Transfer. *Nat. Chem.* **2018**, *10*, 413–419.
- [45] Liu, R.; Zhang, C.; Liang, X.; Liu, J.; Wu, X.; Chen, M. Structural and Dynamic Properties of Solvated Hydroxide and Hydronium Ions in Water from *Ab Initio* Modeling. *J. Chem. Phys.* **2022**, *157*, 024503.

- [46] Zhang, P.; Chen, C.; Feng, M.; Sun, C.; Xu, X. Hydroxide and Hydronium Ions Modulate the Dynamic Evolution of Nitrogen Nanobubbles in Water. *J. Am. Chem. Soc.* **2024**.
- [47] Liu, L.; Tian, Y.; Yang, X.; Liu, C. Mechanistic Insights into Water Autoionization Through Metadynamics Simulation Enhanced by Machine Learning. *Phys. Rev. Lett.* **2023**, *131*, 158001.